Georg R. Pesch, Lars Kiewidt, Fei Du, Michael Baune, Jorg Thöming

Electrodeless dielectrophoresis: Impact of geometry and material on obstacle polarization

Georg R. Pesch
Lars Kiewidt
Fei Du
Michael Baune
Jorg Thöming*

Chemical Engineering, Recovery and Recycling, Department of Production Engineering and Center for Environmental Research and Sustainable Technology, University of Bremen, Bremen, Germany

Received July 8, 2015
Revised September 24, 2015
Accepted September 27, 2015

Research Article

Electrodeless dielectrophoresis: Impact of geometry and material on obstacle polarization

Insulator-based (electrodeless) dielectrophoresis (iDEP) is a promising particle manipulation technique, based on movement of matter in inhomogeneous fields. The inhomogeneity of the field arises because the excitatory field distorts at obstacles (posts). This effect is caused by accumulation of polarization charges at material interfaces. In this study, we utilize a multipole expansion method to investigate the influence of geometry and material on field distortion of posts with arbitrary cross-sections in homogeneous electric fields applied perpendicular to the longitudinal axis of the post. The post then develops a multipole parallel or anti parallel to the excitatory field. The multipoles intensity is defined by the post's structure and material properties and directly influences the DEP particle trapping potential. We analyzed posts with circular and rhombus-shaped cross-sections with different cross-sectional width-to-height ratios and permittivities for their polarization intensity, multipole position, and their particle trapping behavior. A trade-off between high maximum field gradient and high coverage range of the gradient is presented, which is determined by the sharpness of the post's edges. We contribute to the overall understanding of the post polarization mechanism and expect that the results presented will help optimizing the structure of microchannels with arrays of posts for electrodeless DEP application.

Keywords:
Insulating posts / Insulator-based dielectrophoresis / Multipole expansion / Particle Trapping / Polarization

DOI 10.1002/elps.201500313

Additional supporting information may be found in the online version of this article at the publisher's web-site

1 Introduction

Dielectrophoresis (DEP), firstly introduced by Pohl [1] in 1978, describes the movement of charged and uncharged matter in inhomogeneous ac and dc electric fields. It is a promising technology for particle manipulation. Up to now it has mostly been researched and applied in the biomedical industry [2]; e. g. for drug delivery [3], sensing [4], stem cell sorting and discrimination [5], immobilization of single molecules [6], and sorting of cells [7]; as well as in the assembly of nanotubes [8], nanowires [9], and colloidal structures [10]. In industrial scale processes it is investigated as a measure against colloidal membrane fouling in filtration processes [11–14].

DEP movement does not require net charge on the particles and is caused by dielectric polarization of matter (i. e. particles) in electric fields. At material interfaces this polarization is revealed by the formation of macroscopic multipoles. If the excitatory field is *inhomogeneous*, the Coulomb force acting on both sides of the particles is *unequal*, which gives rise to a net dielectrophoretic force acting on the particle [15].

The simple point-dipole approximation uses the field at the center of the particle to evaluate the particle's polarization. The DEP force is then obtained by the first derivative of the field at the same point. It depends on the mediums permittivity, the relative polarizability of the particle in the medium, and on the particle's volume and is driven by the spatial change of the electric field.

Correspondence: Georg R. Pesch, Chemical Engineering, Recovery and Recycling, Department of Production Engineering and Center for Environmental Research and Sustainable Technology, University of Bremen, Bremen, Germany
E-mail: gpesch@uni-bremen.de

Abbreviations: AR, aspect ratio; **DEP**, dielectrophoresis; **FE**, finite element; **iDEP**, insulator-based dielectrophoresis

*Additional corresponding author: Prof. Jorg Thöming
E-mail: thoeming@uni-bremen.de

Colour Online: See the article online to view Figs. 1–7 in colour.

Hence, the movement of very small particles, i. e. nanoparticles, requires vast electric field gradients. They could be achieved either by using technically mature electrode configurations [16] or by placing electric field obstacles in an originally homogeneous field, as it is the case in insulator-based (electrodeless) DEP (iDEP) [17, 18].

The idea, originally developed by Masuda et al. [19] in 1989, relies on the polarization of stationary obstacles or posts in a medium under the presence of an excitatory field. The polarization causes inhomogeneities in the original field, creating high localized gradients, which can be used to either trap particles showing positive DEP at the obstacles or to immobilize particles showing negative DEP at points of equal drag and electric field force in trapping bands [17].

Cummings and Singh [20] identified different flow regimes in an iDEP device with research consisting of a micro channel with an array of insulating posts with circular- and rhombus-shaped cross-sections. Up to today a variety of obstacles have been investigated, including but not limited to circular posts [21], rectangular posts [22, 18], rectangular [23], and triangular [24] constrictions, 3D constrictions [25], filters [26–28], and combinations thereof [29].

Albeit the extensive research progress made in the last decades, a thorough study on the influence of both the obstacle's geometry and material on the induced field gradient has not yet been reported. LaLonde et al. [22] investigated the geometry influence on trapping efficiency in microchannels with insulating posts during trapping DEP operation mode. They found a strong dependence on the required applied voltage for trapping (at constant particle size) with variation of post geometry and cross-sectional aspect ratio. The required voltages where dropping significantly when switching from circular to rectangular posts. Additionally, a decrease of the cross-sectional width-to-length ratio of 1 to 0.67 could further decrease the required voltage by 30 %. This is attributed to higher electric field gradients with increasing sharpness of the post's tip and was also verified by Finite Element simulations. Cho et al. [30] and Braff et al. [25] compared the performance in particle trapping in 3D constrictions against the performance in 2D constrictions by means of simulation and experimental studies. They found a significant increase in particle trapping efficiency when using a 3D constriction compared to the conventional 2D post type constrictions. This is attributed to the increased maximum electric field gradient [30]. Camacho-Alanis et al. [29] investigated streaming and trapping behavior between triangular microposts with different structures placed in the center between two microposts (i.e. single circular nanopost, array of circular nanoposts, and a rectangular nanopost). They reported an increase in particle concentration at the posts when an obstacle is placed between the two microposts, with the rectangular nanopost showing the highest increase, due to an intensified field scattering caused by the sharp edges of the structure compared to the cylindrical obstacles.

Due to the rather complicated design and manufacturing, iDEP devices are not suitable for a high-throughput application. As a much simpler process, in an earlier study, we presented a switchable DEP filtration process for particle separation and recovery [28] that is based on the principle of induced field inhomogeneities. In this filtration process, the choice of filter material is not limited to insulating materials (as iDEP devices usually are due to the common fabrication by soft lithography) and we are free to choose the direction of the original excitatory electric field as we are using pumps and do not rely on EOF (as most iDEP devices do [17]).

The lack of comprehensive studies on the influence of the obstacle's geometry and material on the electric field disturbance, however, poses difficulties to propose an ideal filter design. In the present study, we evaluate the electric field disturbance of obstacles with varying materials (varying ratio of permittivities between outside ε_o and inside permittivity ε_i) and geometries by finite element (FE) simulations (cf. Fig.1A). The analysis is based on the distribution of the electric potential around obstacles that are polarized due to an excitatory field. From the polarization potential field we derive an expression for the electric field gradient. The latter is evaluated in terms of maximum value and decay with distance from the obstacle to survey the relationship between DEP trapping efficiency and obstacle geometry. These obstacles are commonly called posts or "insulating posts" in the iDEP literature. For clarification from now on we stick to this nomenclature. However, we would like to note that our study is not limited to *insulating* posts as we are varying the investigated material combinations.

Our evaluation approach is connatural to the effective moment extraction method described by Green and Jones [31]. First, we establish an analytical expression for the polarization potential of arbitrary structures, based on the approach that the potential due to polarization can be described by a superposition of an infinite number of multipoles. Then, we extract the magnitude of each multipole of several posts with varying geometry and material by FE simulations. An analysis of the contribution of each multipole to the overall electric field inhomogeneity yields the efficiency of each structure for DEP particle trapping.

The presented multipole extraction approach is not aimed to provide a new technique for the numerical description of iDEP devices but serves as a method to *understand* and *quantify* the polarization of posts and to link the polarization to the induced field gradient. We are aware that a full description of the operation of such devices requires modeling a variety of phenomena, such as Joule heating induced temperature changes [32], interparticle interaction [33], and electrokinetic flow [34]. The consideration of above mentioned effects, however, is beyond the scope of this work and they have been purposely excluded, because the present manuscript is aimed to investigate *how* the polarization and hence the electric field gradient is influenced by the geometry and material of the post.

2 Theory

The presented dimensionless investigation is limited to posts with constant cross section and with the excitatory electric

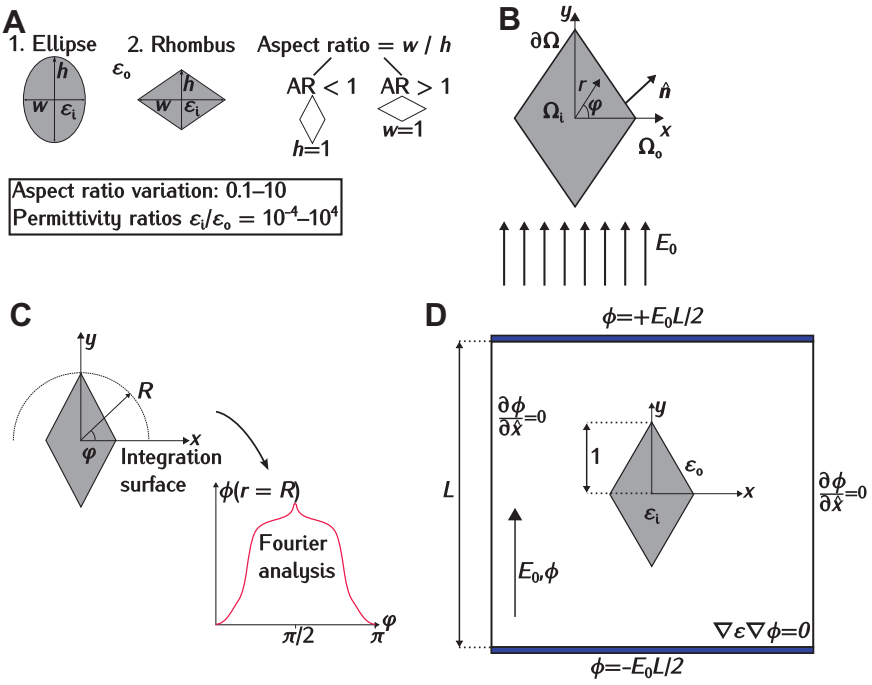

Figure 1. (A) Different post geometries and parameters as investigated in this study. (B) Representation of the model system. The cross-section of the post of domain Ω_i is enclosed by the boundary $\partial\Omega$ and surrounded by the domain Ω_o. The unit normal vector $\hat{n}$ points outwards. (C) The multipole extraction method. (D) Sketch of the simulation domain.

field applied perpendicular to the z-axis of the post. The polarization is then independent of z and two dimensional. Figure 1A shows the two investigated post geometries, viz. a post with elliptic cross-section (1) and rhombus-shaped cross-section (2).

The driving force for DEP is the spatial change of the electric field. With the point-dipole approximation the time-averaged DEP force $\langle \boldsymbol{F}_{\mathrm{DEP}} \rangle$ on a spherical particle with radius a, suspended in a medium with permittivity ε_M can be computed by [15]:

$$\langle \boldsymbol{F}_{\mathrm{DEP}} \rangle = 4\pi a^3 \varepsilon_0 \varepsilon_M \mathrm{re}[K] \left(\boldsymbol{E}_{\mathrm{rms}} \cdot \nabla\right) \boldsymbol{E}_{\mathrm{rms}}, \tag{1}$$

where the dielectric constant $\varepsilon_0 = 8.854 \cdot 10^{-12}$ F/m. The Clausius-Mossotti factor K is a function of the complex permittivities of the particle and the surrounding medium, and the real part re$[K]$ describes the effective polarizability of the particle in the medium [15]:

$$K = \frac{\tilde{\varepsilon}_P - \tilde{\varepsilon}_M}{\tilde{\varepsilon}_P + 2\tilde{\varepsilon}_M}, \tag{2}$$

$$\tilde{\varepsilon} = \varepsilon_r \varepsilon_0 + \frac{\sigma}{i\omega}, \tag{3}$$

with subscripts P and M representing the particle and the medium, respectively. Further, ω is the angular frequency of the applied electric field and $i = \sqrt{-1}$, the imaginary unit. Equation (1) is derived on the assumption of a spherical particle whose diameter is much smaller compared to the spatial change of the electric field and thus underestimates the forces on nonspherical particles and in regions of high spatial field change [35]. More elaborate approaches include higher order polarization terms (and higher order derivatives of the field) [36] or rely on the evaluation of the Maxwell-Stress-Tensor [37], which is the most rigorous approach for DEP force calculation.

The $\boldsymbol{F}_{\mathrm{DEP}}$ can point either *in direction* of the $\boldsymbol{E}$ field gradient or *against* it, depending on the sign of re$[K]$. If re$[K]$ is positive (negative) $\boldsymbol{F}_{\mathrm{DEP}}$ points toward strong (weak) electric field regions, referred to as positive (negative) DEP.

In electrodeless DEP, the required field change is caused by polarization charge induced inhomogeneities at material interfaces. To adequately describe the polarization, an expression for the potential field and the electric field induced by polarized posts is derived.

2.1 Computation of electric potential and electric field

The calculation of electric fields requires solving Poisson's equation for the electric potential ϕ [38]:

$$\nabla^2 \phi = \frac{\rho}{\varepsilon}, \tag{4}$$

with ρ being the space charge density and ε the permittivity.

The electric field $\boldsymbol{E}$ is calculated from the electric potential by

$$\boldsymbol{E} = -\nabla\phi. \tag{5}$$

Equation (4) is general and applicable for all linear and isotropic materials.

In case of time-varying harmonic fields (ac fields) with angular frequency ω, ρ can be substituted in Eq. (4) by applying Ohm's law and charge conservation [15]:

$$\nabla\tilde{\varepsilon}\nabla\phi = 0. \tag{6}$$

This is the complex Poisson's equation. For simplification, and without loss of generality, in the present study we ignore the complex part of Eq. (6). Then, Eq. (6) reduces to the material-dependent Laplace equation, which is only valid for perfect nonconductive and nondispersive dielectrics in the absence of charges:

$$\nabla\varepsilon\nabla\phi = 0. \tag{7}$$

In this case, the electric field distribution depends only on one material constant (ε), thus simplifying the analysis. We like to note that the method is similarly applicable for the complex Poisson's equation by replacing all ε with $\tilde{\varepsilon}$. The real part of the polarization coefficients (see Section 2.2) then gives the in-phase polarization whereas the complex part gives the out-of-phase loss.

2.2 Derivation of the multipole expansion in cylindrical coordinates

Here, we study the polarization of posts in the presence of an external electric field E_0, which is applied perpendicular to the z-axis. Furthermore, the post's height is assumed to be much larger than its radial extension.

The geometry is then given in 2D polar coordinates (r, φ) (Fig. 1B). It is convenient to define two separate domains Ω_i and Ω_o, which describe the inner part of the post and the surrounding medium, respectively. The domains are separated by $\partial\Omega$ (Fig. 1B). Both domains separately have to fulfill Eq. (7), so that ε becomes constant in the entire domain and can be eliminated from Eq. (7):

$$\Delta\phi = 0. \tag{8}$$

This yields two separate potentials, the inside and outside potential, ϕ_i and ϕ_o, respectively, which are only valid in their respective domains.

The potentials are coupled at $\partial\Omega$ by [39]

$$\begin{cases} \varepsilon_i \frac{\partial\phi_i}{\partial\hat{\boldsymbol{n}}}\Big|_{\forall(r,\varphi)\in\partial\Omega} = \varepsilon_o \frac{\partial\phi_o}{\partial\hat{\boldsymbol{n}}}\Big|_{\forall(r,\varphi)\in\partial\Omega} \\ \frac{\partial\phi_i}{\partial\hat{\boldsymbol{t}}}\Big|_{\forall(r,\varphi)\in\partial\Omega} = \frac{\partial\phi_o}{\partial\hat{\boldsymbol{t}}}\Big|_{\forall(r,\varphi)\in\partial\Omega} \\ \phi_i|_{\forall(r,\varphi)\in\partial\Omega} = \phi_o|_{\forall(r,\varphi)\in\partial\Omega} \end{cases} \tag{9}$$

with $\hat{\boldsymbol{n}}$ being the outward pointing normal unit vector and $\hat{\boldsymbol{t}}$ being the perpendicular tangential unit vector.

A solution for Eq. (8) is obtained by finding a separated-variable solution and then enforcing the boundary conditions,

$$\lim_{r\to\infty} \phi_o(r, \varphi) = E_0 r \sin\varphi, \tag{10a}$$

$$\lim_{r\to 0} \phi_i(r, \varphi) \neq 0, \tag{10b}$$

and assuming rotational symmetry:

$$\phi_o(r, \varphi) = E_0 r \sin\varphi + \sum_{n=1}^{\infty} \frac{p_n \sin(n\varphi)}{r^n}, \tag{11a}$$

$$\phi_i(r, \varphi) = \sum_{n=1}^{\infty} r^n w_n \sin(n\varphi). \tag{11b}$$

Here, p_n and w_n are constants. The outside potential ϕ_o is thus the sum of the applied potential that is causing E_0, $\phi_{appl} = E_0 r \sin\varphi$, and the polarization potential of the post, ϕ_{pol}: $\phi_o = \phi_{appl} + \phi_{pol}$. Additionally, ϕ_{pol} is expressed as a superposition of an infinite amount of multipoles with fading magnitude as expressed by the polarization coefficients p_n.

For an arbitrary but fixed $r = R$ (with $R \geq 1$), the polarization potential can be expressed as a Fourier series with respect to φ and the Fourier coefficients p_n (Fig. 1C). We can thus extract the p_n from any given solution of the polarization potential (i.e. FE simulation) by integration,

$$p_n = \frac{2}{\pi} \int_0^{\pi} \phi_{pol}(\varphi, R) \sin(n\varphi) \mathrm{d}\varphi. \tag{12}$$

After obtaining the multipole coefficients, it is an easy exercise to find the force exerted on a spherical particle in the vicinity of a polarized structure by differentiating Eq. (11a) twice:

$$\boldsymbol{F}_{DEP} \sim (\boldsymbol{E}\cdot\nabla)\,\boldsymbol{E} = \begin{pmatrix} \frac{\partial^2\phi_o}{\partial x^2}\frac{\partial\phi_o}{\partial x} + \frac{\partial^2\phi_o}{\partial x\partial y}\frac{\partial\phi_o}{\partial y} \\ \frac{\partial^2\phi_o}{\partial y\partial x}\frac{\partial\phi_o}{\partial x} + \frac{\partial^2\phi_o}{\partial y^2}\frac{\partial\phi_o}{\partial y} \end{pmatrix} = \begin{pmatrix} -\sum_{n=1}^{\infty}\sum_{k=1}^{\infty} \frac{kn(n+1)}{r^{k+n+3}} p_n p_k \cos\big((k-n-1)\varphi\big) - \sum_{n=1}^{\infty} \frac{n(n+1)}{r^{n+2}} E_0 p_n \cos\big((n+2)\varphi\big) \\ \sum_{n=1}^{\infty}\sum_{k=1}^{\infty} \frac{kn(n+1)}{r^{k+n+3}} p_n p_k \sin\big((k-n-1)\varphi\big) - \sum_{n=1}^{\infty} \frac{n(n+1)}{r^{n+2}} E_0 p_n \sin\big((n+2)\varphi\big) \end{pmatrix}. \tag{13}$$

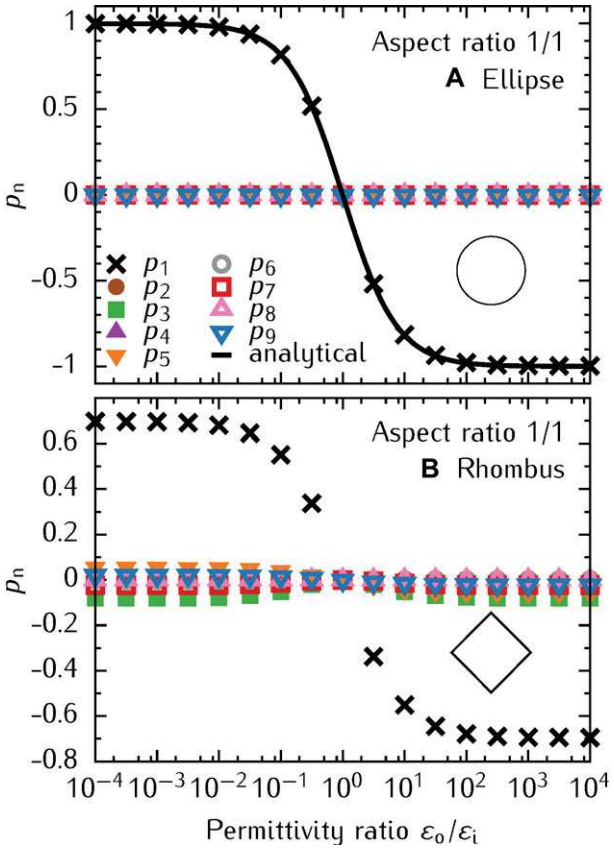

Figure 2. First nine multipole coefficients p_n (points) of a post with (A) elliptical (circular) and (B) rhombus-shaped cross section for different permittivity ratio $\varepsilon_o/\varepsilon_i$. Both have an aspect ratio (AR) of 1. Analytical solution for p_1 of a circle is shown as a solid line for comparison.

Equation (13) describes the DEP force in (x, y) directions caused by the polarization of a postexpressed in (r, φ) coordinates. Cartesian (x, y) coordinates have been introduced because of the usually employed rectangular microchannel geometry. The relations between (x, y) and (r, φ) are $\varphi = \text{atan2}(y, x)$ and $r = \sqrt{x^2 + y^2}$.

The double sum is present because the electric field has to be evaluated twice to find the force. The polarization of the spherical particle is evaluated with the value of the electric field at the center of the particle. Then, the electric field gradient at that point is used to calculate the force exerted by the inhomogeneous field on the polarized particle. By iterating through the sum we thereby find the force exerted by the electric field gradient caused by the n-th multipole (p_n) of the post on a particle that is polarized by the electric field of the k-th multipole (p_k) of the post. The two single sums on the right describe the force caused by the n-th multipole of the post on a particle polarized by the homogeneous applied electric field E_0. The DEP force $\boldsymbol{F}_{\text{DEP}}$ hence depends on the position (r, φ) of the particle with respect to the post and on the magnitude of the post's polarization coefficients p_n (and p_k).

3 Method

The polarization potential of the posts has been obtained by performing 2D dimensionless FE simulations in Cartesian coordinates. The post is placed in the center of the rectangular simulation surface of size $L \times L$ (Fig. 1D). Posts with constant rhombus-shaped and elliptical cross sections have been investigated. The aspect ratio (AR), i. e. the ratio of the width w and height h, has been varied between 0.1 and 10. The longer dimension of the post was fixed to be one, so that a post with AR < 1 has $h = 1$ and one with AR > 1 has $w = 1$ (cf. Fig. 1).

A simulation surface size of $L = 50$ turned out to be sufficiently large for the simulation result being independent of the boundary. To simulate the polarization of the post the material-dependent Laplace equation (Eq. (7)) has to be solved. Dirichlet boundary conditions are applied at the electrodes (top and bottom),

$$\phi(x, y)\big|_{\forall y = \mp L/2} = \pm \frac{E_0 L}{2}, \tag{14}$$

whereas Neumann boundary conditions are applied at the insulating boundaries (left and right) of the simulation surface:

$$\left.\frac{\partial \phi(x, y)}{\partial \hat{\boldsymbol{x}}}\right|_{\forall x = \pm L/2} = 0. \tag{15}$$

The applied field is E_0 and $\hat{\boldsymbol{x}}$ represents the unit vector in x direction (i. e., towards the insulating boundary). An electric field of strength $E_0 = 1$ has been applied in order to excite the post polarization.

Simulations have been performed using the open-source FEniCS project [40] operated with an IPython front-end including NumPy and SciPy. The generation of geometry and mesh was obtained by using the open-source tool GMSH. We defined four points of minimum mesh size, viz. the four corners of the structure, and expanded the mesh towards the boundaries of the simulation surface. To verify mesh-independent results, the first 1000 multipoles for every structure have been extracted while reducing the maximum mesh size step-by-step at the four points until a stable sum is reached. The final mesh consisted of approx. 2 000 000–4 000 000 elements depending on the geometry and aspect ratio.

The polarization coefficients have been extracted by firstly subtracting the applied potential from the FE result to find the potential caused only by the polarization. In a second step a trapezoidal method for integration (NumPy's `trapz` function) was used to find p_n for different integration radii R.

4 Results and discussion

4.1 Polarization

Typical iDEP devices are made of PDMS. Assuming an ac excitatory field and $\varepsilon_{\text{PDMS}} = 2.3$ and $\sigma_{\text{PDMS}} = 2.5 \cdot 10^{-14}$ S/m,

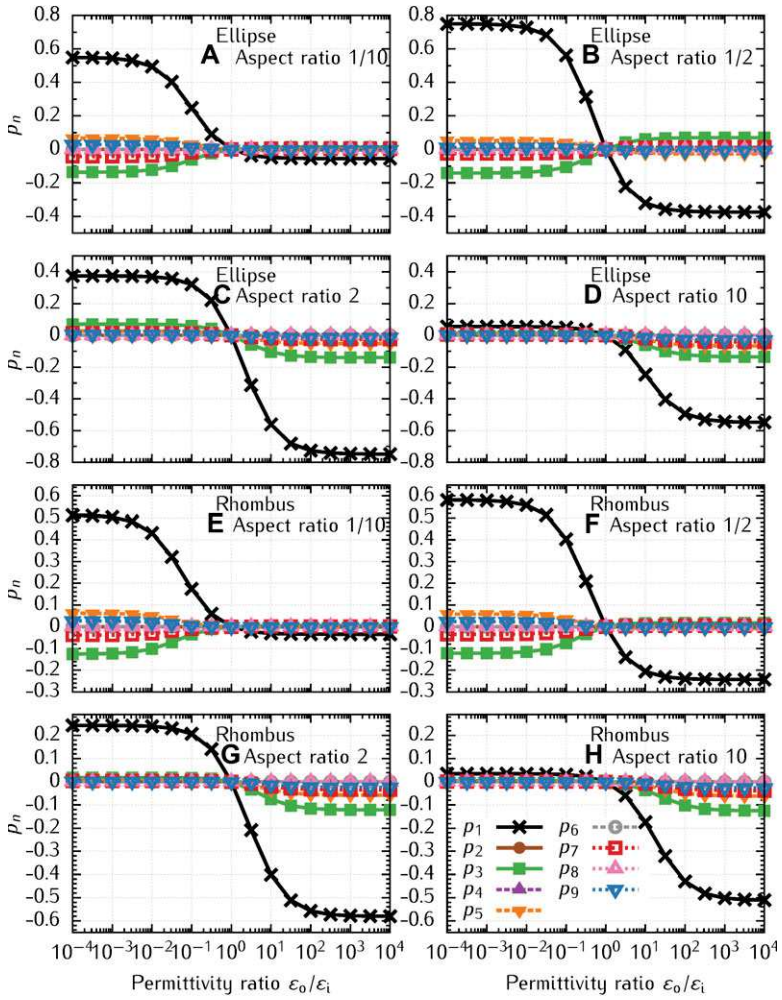

Figure 3. First nine multipole coefficients p_n of posts with elliptical (A–D) and rhombus-shaped (E–H) cross section for different permittivity ratios $\varepsilon_o/\varepsilon_i$ and varying aspect ratios: (A, E) 1/10, (B, F) 1/2, (C, G) 2, (D, H) 10.

the real part of the complex permittivity ratio for insulating posts in DI water is, depending on ω, between $2.2 \cdot 10^8$ (low frequency limit) and $3.6 \cdot 10^1$ (high frequency limit). Figure 2 shows the first nine multipole coefficients p_n (points) of a post with elliptic (circular) (A) and rhombus-shaped (B) cross section with an aspect ratio of one and different permittivity ratios $\varepsilon_o/\varepsilon_i$. For a circular (elliptical with AR 1) post, only the first coefficient p_1 has a nonzero value ranging from 1 for a material that has a much higher permittivity ε_i than the surrounding medium to −1 for materials that have a much lower permittivity compared to the medium permittivity ε_o. All higher order coefficients are zero within numerical accuracy. The analytical solution for p_1 of an ellipse is plotted for comparison as a solid black line. It can be found by matching Eq. (11a) with Eq. (11b) at $\partial\Omega$ using the appropriate boundary conditions:

$$p_1 = \frac{1 - \varepsilon_o/\varepsilon_i}{1 + \varepsilon_o/\varepsilon_i}. \tag{16}$$

The numerical results show excellent agreement with the analytical solution.

For the rhombus-shaped post (Fig. 2B) the first-order coefficient is ranging from 0.7 to −0.7 and is thus 30% lower than the p_1 of the ellipse. The odd higher order coefficients, however, have a value different from zero, whereas the even coefficients remain zero. For post materials with $\varepsilon_i > \varepsilon_o$, every second odd coefficient changes the sign, whereas all coefficients have the same sign for $\varepsilon_i < \varepsilon_o$. Additionally, the magnitude of the coefficients is equal at both limits.

Hence, a post with circular cross-section only develops a dipole polarization (as only p_1 has a nonzero value) in a homogeneous electric field. With deviation from the circular cross-section (e.g. a rhombus-shaped) higher order multipoles arise (and the p_n for $n > 1$ have nonzero values).

Figure 3A–D shows the development of the first nine multipole coefficients with the permittivity ratio $\varepsilon_o/\varepsilon_i$ of a post with elliptical cross section and different aspect ratios. For AR > 1 (Fig. 3C and D), all coefficients have the same sign with all even coefficients being zero. All odd coefficients, however, are negative for $\varepsilon_i < \varepsilon_o$ and positive for $\varepsilon_o < \varepsilon_i$. The coefficients generally have a lower magnitude if $\varepsilon_i > \varepsilon_o$ compared to $\varepsilon_i < \varepsilon_o$. With increasing deviation of AR from unity, the first order coefficient decreases in magnitude whereas

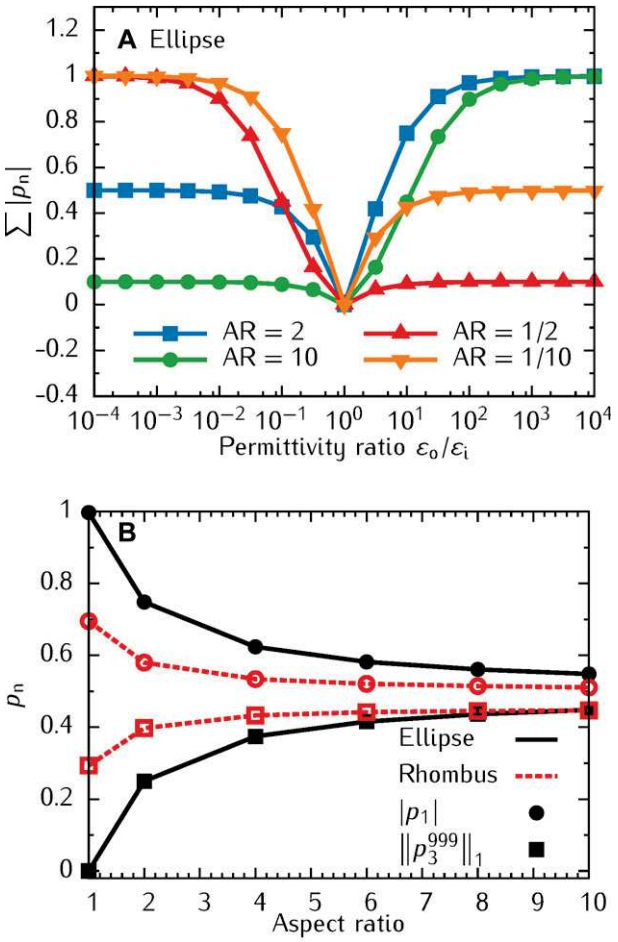

Figure 4. (A) L^1-norm of the first 1000 multipole coefficients $\|p_n\|_1$ for different aspect and permittivity ratios $\varepsilon_o/\varepsilon_i$ of a post with elliptical cross section. (B) Comparison of $|p_1|$ and the sum of all higher order coefficients up to $n = 1000$, $\|p_3^{999}\|_1 = \sum_3^{999} |p_n|$, for a post with elliptical cross section (solid line) and rhombus-shaped cross section (dashed line) as a function of aspect ratio at a permittivity ratio of $\varepsilon_o/\varepsilon_i = 10^4$.

the higher coefficients increase in magnitude. This is hard to infer from Fig. 3, but is evident from Fig. 4B. Similar trends can be found for AR < 1 (Fig. 3A and B). All even coefficients are zero with the difference that every other odd coefficient changes signs from negative to positive and vice versa. In contrast to AR > 1, all multipole coefficients have larger magnitude if the post permittivity is higher than the medium permittivity, $\varepsilon_i > \varepsilon_o$. Again, the first-order coefficient decreases in magnitude with increasing variation of AR from unity, i.e. with decreasing AR, whereas the higher order coefficients increase in magnitude. Analogous, the first nine multipole coefficients as a function of $\varepsilon_o/\varepsilon_i$ for posts with a rhombus-shaped cross section and varying aspect ratios are plotted in Fig. 3E–H, from which similar trends to the elliptical posts (A–D) can be inferred.

Generally, the magnitude of each coefficient, $|p_n|$, for a post with a given aspect ratio and at a given permittivity ratio is identical to the magnitude of the coefficient of a post with the inverse permittivity ratio $\varepsilon_i/\varepsilon_o$ and the inverse aspect ratio 1/AR (which results in a 90° rotation of the post around the origin). This can also be inferred from Fig. 4A, which shows the L^1-norm of the first 1 000 coefficients of a post with elliptical cross-section for different permittivity and aspect ratios. The sum of the magnitude of the coefficients for the post with AR 2 and 10 is mirrored at $\varepsilon_o/\varepsilon_i = 1$ by the posts with AR 1/2 and 1/10. The same holds for posts with rhombus-shaped cross-section (not plotted).

Figure 4B shows the development of the first-order coefficient $|p_1|$ and the L^1-norm of all higher order coefficients $\|p_3^{999}\|_1 = \sum_3^{999} |p_n|$ with aspect ratio at a fixed permittivity ratio of $\varepsilon_o/\varepsilon_i = 10^4$. For a post with elliptical cross section (solid line), the magnitude of the first-order coefficient (circles) is 1 at an aspect ratio of 1 and is decreasing in magnitude with aspect ratio to a value of 0.55. The sum of the higher order coefficients (rectangles) is 0 at AR $= 1$ and increasing in magnitude with AR up to a value of 0.48 at AR $= 10$.

The $|p_1|$ of the rhombus-shaped post (dashed line, circles) is lower for all investigated aspect ratios compared to posts with elliptical cross-section. Similarly, the 1-norm of the higher order coefficients (rectangles) is higher for all AR.

A post with circular cross-section (ellipse with AR $= 1$) only shows dipole polarization. When AR deviates from unity, higher order multipoles arise. With increasing deviation, the distribution of the overall polarization shifts from the dipole polarization to higher order multipoles. The effect is more pronounced for posts with rhombus-shaped cross sections, since a rhombus is naturally a different geometry than an ellipse. Here, posts with AR $= 1$ cross-section already show higher order polarization.

We will now deduce several rules concerning the dielectrophoretic force exerted by the polarization field from the distribution of multipoles regarding aspect ratio, permittivity ratio, and geometry of the post.

The charge distribution caused by the polarization, i.e. the resulting potential field, always shows two extrema found parallel to the applied electric field.

The magnitude of the polarization can be inferred from the magnitude and sign of the polarization coefficients, which are directly related to the permittivity ratio. Posts having the same permittivity as the surrounding medium show no polarization (as all coefficients are 0) and they are "invisible" to the excitatory field. With increasing deviation of the permittivity ratio from unity the posts will experience more polarization until an observable (e.g. in Fig. 3) maximum is reached at $\varepsilon_o/\varepsilon_i \approx 10^{\pm 4}$. The position of the extrema of the resulting $\boldsymbol{E}$-field due to polarization depends on the sign of the first-order coefficient. If the first-order coefficient is positive, $\boldsymbol{E}$ has two maxima, found at the two tips of the post parallel to the applied electric field, and two minima, found perpendicular to the applied field (cf. Fig. 5, top row). Vice versa, if the first-order coefficient is negative, the two maxima are located at points perpendicular to the applied electric field and the minima are located at points parallel to the applied field (cf. Fig. 5, bottom row).

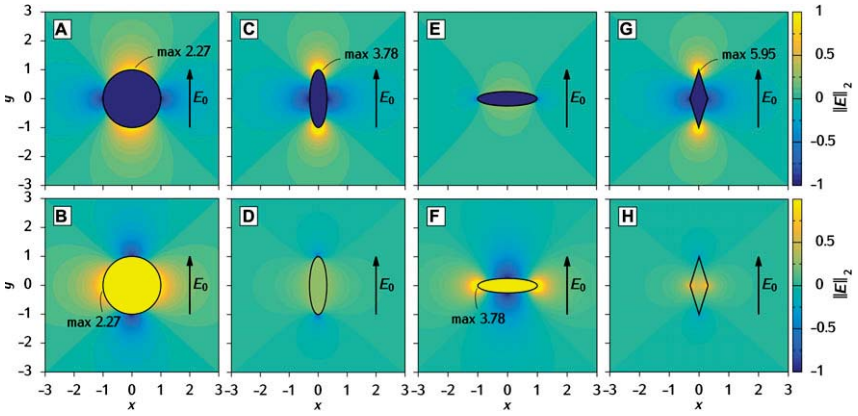

Figure 5. Electric field magnitude $\|E\|_2$ as generated by polarized posts with circular cross section (A, B), elliptical cross section with AR = 1/6 (C, D), elliptical cross section with AR = 6 (E, F) and rhombus-shaped cross-section with AR = 1/6 (G, H) in an electric field of $E_0 = 1$. (A, C, E, G) Permittivity of the surrounding medium ε_o is 10 000× smaller than the permittivity of the post ε_i and (B, D, F, H) ε_o is 10 000× higher than ε_i. Due to the large differences in average and maximum values, the color range has been fixed between −1 and 1 and the maximum values are given as numbers.

The influence of the higher order coefficients on the resulting $\boldsymbol{E}$-field depends on their sign. Two cases have to be considered: In the first case, all higher order coefficients have the same as p_1 (AR > 1): Then, the higher-order multipoles strengthen an $\boldsymbol{E}$-field whose maxima are located at two points perpendicular to the applied electric field ($\varepsilon_o/\varepsilon_i > 1$, AR > 1, Fig. 5f). On the other hand, they are effectively reducing an $\boldsymbol{E}$-field whose maxima are found at two points parallel to the applied electric field ($\varepsilon_o/\varepsilon_i < 1$, AR > 1, Fig. 5E). In the second case, all coefficients are changing signs (AR < 1). Then, the higher order multipoles will intensify an $\boldsymbol{E}$-field that has its maxima parallel to the excitatory field ($\varepsilon_o/\varepsilon_i < 1$, AR < 1, Fig. 5C and G) and weaken an $\boldsymbol{E}$-field, which has its maxima perpendicular to the applied electric field ($\varepsilon_o/\varepsilon_i > 1$, AR < 1, Fig. 5D and H).

Hence, a post that has a higher permittivity than the surrounding medium ($\varepsilon_i > \varepsilon_o$) should be placed with the longer axis aligned parallel to the applied electric field (AR < 1, case 2). This will lead to strong electric fields and thus strong gradients at the two edges parallel to the applied electric field. The opposite holds for posts with lower permittivity than the surrounding medium ($\varepsilon_i < \varepsilon_o$): Maximum polarization and electric field gradients are achieved if the longer axis is aligned perpendicular to the electric field (AR > 1, case 1). Points of maximum electric field are then located at the two edges perpendicular to the applied electric field.

In other words, structures with an AR different from unity always show two "soft" edges and two "sharp" edges. The "sharp" edges should always be located at the two points with the maximum electric field (as defined by $\varepsilon_o/\varepsilon_i$, Fig. 5).

Differently from the polarization of spherical particles as expressed by the well-known Clausius–Mossotti factor, the polarization intensity of quasi 2D posts (as presented in this study) is independent of the polarization direction (which is defined by $\varepsilon_o/\varepsilon_i$). The Clausius–Mossotti factor, which is the first-order polarization coefficient of spherical particles, is bound between −0.5 and 1. Thus, particles that have a permittivity much higher than the surrounding medium's permittivity are better polarizable than particles that have a much lower permittivity than the surrounding medium's permittivity (since $|1| > |-0.5|$). Hence, the polarization intensity is dependent on the polarization direction. For posts (cylinder-like structures), the first-order coefficient is bound between −1 and 1, leading to the same polarization in both cases. A post with an aspect ratio different from unity shows equal polarization compared to a post with the inverse permittivity ratio, rotated by 90° around the point of origin (cf. Fig. 4A and compare Fig. 5C and F).

Additionally, comparing Fig. 5A, C, and G reveals that with increasing "sharpness" of the tip (from A to G) the maximum value of the electric field magnitude increases. The high values are, however, more localized with increasing "sharnpess" (cf. Fig. 5C and G, the bright yellow circle indicating values above 1 becomes smaller).

4.2 Influence on DEP force

Intensity and range of the dielectrophoretic force exerted by the polarized posts depends on the aspect ratio. As it can be inferred from Eq. (13), the force exerted on a spherical particle in vicinity of the post depends on $(n(n+1))r^{-n-2}$, with n being the order of the multipole coefficient. It is evident that the exerted force caused by the multipole is, with increasing order n of the multipole coefficients, much higher in the near vicinity of the post (i.e. r is slightly greater than h) but decays more rapidly due to the inverse power dependency of $\boldsymbol{F}_{\mathrm{DEP}}$ on r. Thus, posts with lower magnitude first-order coefficient but high magnitude higher order coefficients (AR very different from unity) cause greater DEP force in the vicinity of the post than posts with low higher order coefficients and a first-order coefficient close to unity (AR almost unity). This, however, comes along with decreased range of the force.

Hence, with increasing "sharpness" of the post's edge (increasing deviation of AR from unity) the exerted DEP force increases in close vicinity to the edge. This allows very effective but only *localized* trapping of particles close to the post, a fact that has been observed several times in the literature [22, 41, 42]. If the posts, however, are spaced widely, the efficiency for particle trapping will be reduced due to the strong localization of the gradient.

This can also be inferred from Fig. 6, which shows the variation of the force magnitude $\bar{F}_{\mathrm{DEP}}$ with distance $\bar{r}$ at

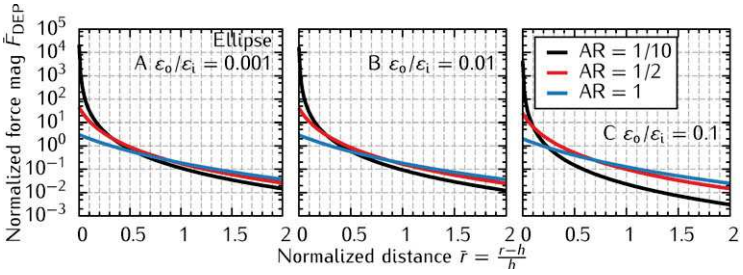

Figure 6. Normalized DEP force magnitude $\bar{F}_{DEP} = F_{DEP}/(4\pi a^3 \varepsilon_p \mathrm{re}[K])$ as a function of the normalized distance from the post $\bar{r} = (r - h)/h$ for three different permittivity ratios $\varepsilon_i/\varepsilon_o = 10^{-3}$, 10^{-2}, and 10^{-1} and three different aspect ratios 1/10, 1/2, and 1 at an angle of $\varphi = \pi/2$.

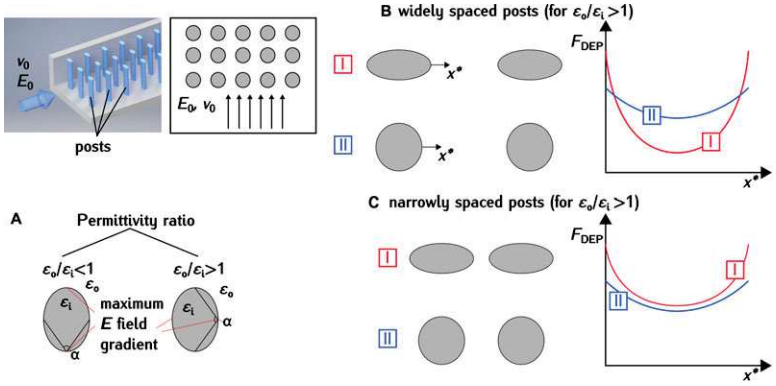

Figure 7. (A) The position of the maximum induced field gradient dependents on the material properties (i.e. permittivity ratio). Its strength depends on the angle α, which defines the sharpness of the tip. (B, C) DEP force between (B) widely and (C) narrowly spaced posts in case of $\varepsilon_o > \varepsilon_i$ (qualitative). The dimensionless coordinate between the posts is $x^* = x/d$ where d is the distance between the posts. Posts with sharp tips (α close to 0) show high maximum DEP forces, but also a fast decay with x^*. Posts with soft tips (α close to $\pi/2$) show a more equal force distribution.

$\varphi = \pi/2$ for three different aspect ratios and three different permittivity ratios. For all investigated permittivity ratios, the force close to the post is the highest for AR = 1/10 and the lowest for AR = 1. The decay of $\bar{F}_{DEP}$ with $\bar{r}$ (slope of $\bar{F}_{DEP}(\bar{r})$), however, is also the highest for AR = 1/10, followed by AR = 1/2. Posts with AR = 1 show the lowest slope. Therefore, at some distance $\bar{r}^*$ from the post, the post with AR = 1/2 outperforms the AR = 1/10 post in terms of exerted DEP force. When looking at points even farther away from the structure, the post with AR = 1 exerts the highest force, followed by the post with AR = 1/2 and the post with AR = 1/10 shows the lowest force. The sequence of $\bar{F}_{DEP}$ with AR is thus reversed. The distance at which the forces intersect each other is shifted closer toward the posts (lower values of $\bar{r}$) when the permittivity ratio is closer to unity. In addition, the difference in force between the three investigated posts at larger $\bar{r}$ is higher at permittivity ratios close to unity.

This shows the necessity to make a trade-off between intensity (maximum force exerted by the polarized structure) and reach (decay of the force) of the trapping by polarized posts and limits the often-made claim [22, 41, 42] that posts or obstacles with sharper tips show generally better trapping efficiency.

We have verified the deployed algorithm for the derivation of the potential and the force against results of Moncada-Hernandez et al. [43] for the experimental and simulated trapping of yeast and *E. coli* cells. An identical analysis framework and the same values for the electrokinetic properties of the cells and the dimensions of the microchannel have been used.

That is, we have assumed nonperfect dielectrics and thus replaced the real permittivity ratio $\varepsilon_o/\varepsilon_i$ by the complex permittivity ratio $\tilde{\varepsilon}_o/\tilde{\varepsilon}_i$ (see Section 2.1). Since we assumed a dc electric field, the angular frequency of the field $\omega \to 0$; then, the complex permittivity ratio reduces to σ_o/σ_i, the ratio between the medium's and the post's *conductivity*. The 0.5 mM KH_2PO_4 solution used in ref. [43] has a measured conductivity of $\sigma_o = 5 \cdot 10^{-4}$ S/m. Assuming a postconductivity of $\sigma_i = 2.5 \cdot 10^{-14}$ S/m (typical value for PDMS) the conductivity ratio is $2 \cdot 10^{10}$.

The trapping regions have been derived by employing the well-known trapping condition. The condition states that the ratio between the electrokinetic forces in one direction (which is the sum of electroosmosis and electrophoresis) have to be smaller than the dielectrophoretic forces in the opposite direction to achieve trapping. This is expressed by the electrokinetic and dielectrophoretic mobilities of the particles, μ_{EK} and μ_{DEP}, respectively:

$$\frac{\mu_{DEP} \nabla |\boldsymbol{E}|^2}{\mu_{EK} \boldsymbol{E}^2} \boldsymbol{E} > 1. \tag{17}$$

The resultant trapping regions agree very well with the results from ref. [43]. A somewhat more detailed description of the procedure and the results could be found in the Supporting Documents [44].

5 Concluding remarks

In this study, we used a multipole expansion method to describe and quantify the polarization potential of posts with arbitrary cross sections in a given homogeneous excitatory field. More specifically, we evaluated the influence of the cross-sectional geometry, the cross-sectional aspect ratio and the material combinations (of the post and the medium) on the electric polarization, the resulting field disturbance,

and the potential for DEP particle trapping. The polarization potential of posts in 2D polar coordinates is given by a Fourier series with respect to the azimuth at a fixed radius. The coefficients were extracted from FEM simulations of polarization potential by integration.

The polarization of the post depends on the ratio of the medium's and the post's permittivity. The magnitude of the polarization is increasing with deviation of the permittivity ratio from unity. When the post's permittivity is higher (lower) than the one of the surrounding medium, the two points of maximum electric field gradient appear at the boundaries of the obstacle parallel (perpendicular) to the excitatory field. Further, the alignment of the post with respect to the excitatory field defines the polarization. To achieve high electric field gradients, posts, whose cross section show an aspect ratio different from unity, should be aligned with the longer axis parallel to the excitatory field if the post material's permittivity is higher than that of the surrounding medium. Vice versa, the longer axis should be aligned perpendicular to the field in case the medium's permittivity is higher than the post material's permittivity. Finally, the overall magnitude and the decay with distance from the post of the electric field gradient is defined by sharpness of the tip that is located at the maximum gradients position (angle α in Fig. 7A). With decreasing α, the gradient becomes more localized (faster decay with r) but also stronger in the vicinity of the structure (r slightly greater than h). If α is close $\pi/2$ the gradient's overall value in the vicinity of the tip, but also the slope with respect to r, are lower. This leads to overall lower but broader distribution of the gradient. If $\alpha > \pi/2$, the post does not show efficient particle trapping behavior. This requires a trade-off between intensity and reach of DEP force that has to be solved for the individual application and extends the claim that pointy tips always lead to higher forces (cf. Fig. 7B, C). In the future we will apply this method to evaluate single particle trapping by single posts using force balance and equation of motion. Based on the single particle and single post behavior we expect to be able to calculate the overall efficiency of post ensembles. This knowledge will be applied to deduce design rules for real porous structures for dielectrophoretical particle filtration.

G.P. and L.K. would like to thank the German Research Foundation for financial support through the Research Traning Group (GRK 1860) "Micro-, meso- and macroporous nonmetallic Materials: Fundamentals and Application."

The authors declare no conflict of interest.

6 References

[1] Pohl, A.H., *Dielectrophoresis*. Cambridge University Press, London, New York, Melbourne 1978.

[2] Pethig, R., *Biomicrofluidics* 2010, *4*, 022811.

[3] Pethig, R., *Adv. Drug Deliv. Rev*. 2013, *65*, 1589–1599.

[4] Sonnenberg, A., Marciniak, J.Y., Skowronski, E. A., Manouchehri, S., Rassenti, L., Ghia, E. M., Widhopf, G. F., Kipps, T. J., Heller, M.J., *Electrophoresis* 2014, *35*, 1828–1836.

[5] Velugotla, S., Pells, S., Mjoseng, H. K., Duffy, C. R. E., Smith, S., De Sousa, P., Pethig, R., *Biomicrofluidics* 2012, *6*, 044113.

[6] Hölzel, R., Calander, N., Chiragwandi, Z., Willander, M., Bier, F., *Phys. Rev. Lett*. 2005, *95*, 128102.

[7] Braschler, T., Demierre, N., Nascimento, E., Silva, T., Oliva, A. G., Renaud, P., *Lab Chip*. 2008, *8*, 280–286.

[8] Krupke, R., Hennrich, F., Weber, H. B., Kappes, M. M., Löhneysen, V. H., *Nano Lett*. 2003, *3*, 1019–1023.

[9] Hughes, M. P., *Nanoelectromechanics in Engineering and Biology*, 1st ed. CRC Press, Boca Raton 2002 p. 164–168.

[10] Bharti, B. and Velev, O.D., *Langmuir* 2015, *31*, 7897–7908.

[11] Molla, S. and Bhattacharjee, S., *Langmuir* 2007, *23*, 10618–10627.

[12] Du, F., Hawari, A., Baune, M., Thöming, J., *J. Memb. Sci*. 2009, *336*, 71–78.

[13] Du, F., Ciaciuch, P., Bohlen, S., Wang, Y., Baune, M., Thöming, J., *J. Memb. Sci*. 2013, *448*, 256–261.

[14] Hawari, A., Du, F., Baune, M., Thöming, J., *J. Environ. Sci*. 2015, *29*, 139–145.

[15] Morgan, H. and Green, N. G, *AC Electrokinetics: colloids and nanoparticles*, 1st ed. Research Studies Press, Baldock 2002.

[16] Wang, Y., Du, F., Baune, M., Thöming, J., *Microfluid Nanofluidics* 2014, *17*, 499–507.

[17] Srivastava, S.K., Gencoglu, A., Minerick, A.R., *Anal. Bioanal. Chem*. 2011, *399*, 301–321.

[18] Lapizco-Encinas, B.H., Simmons, B.A., Cummings, E.B., Fintschenko, Y., *Anal. Chem*. 2004, *76*, 1571–1579.

[19] Masuda, S., Washizu, M., Nanba, T., *IEEE Trans. Ind. Appl*. 1989, *25*, 732–737.

[20] Cummings, E.B., Singh, A.K., *Anal. Chem*. 2003, *75*, 4724–4731.

[21] Gallo-Villanueva, R.C., Pérez-González, V.H., Davalos, R.V., Lapizco-Encinas, B.H., *Electrophoresis* 2011, *32*, 2456–2465.

[22] LaLonde, A., Gencoglu, A., Romero-Creel, M. F., Koppula, K. S., Lapizco-Encinas, B.H., *J. Chromatogr. A* 2014, *1344*, 99–108.

[23] Hawkins, B. G. and Kirby, B. J., *Electrophoresis* 2010, *31*, 3622–3633.

[24] Swami, N., Chou, C.-F., Ramamurthy, V., Chaurey, V., *Lab Chip* 2009, *9*, 3212–3220.

[25] Braff, W. A., Pignier, A., Buie, C. R., *Lab Chip* 2012, *12*, 1327–1331.

[26] Suehiro, J. S. J., Zhou, G. Z. G., Imamura, M., Hara, M., *IEEE Trans. Ind. Appl*. 2003, *39*, 1514–1521.

[27] Iliescu, C., Xu, G., Loe, F. C., Ong, P. L., Tay, F. E. H., *Electrophoresis* 2007, *28*, 1107–1114.

[28] Pesch, G.R., Du, F., Schwientek, U., Gehrmeyer, C., Maurer, A., Thöming, J., Baune, M., *Sep. Purif. Technol*. 2014, *132*, 728–735.

[29] Camacho-Alanis, F., Gan, L., and Ros, A., *Sens. Actuators. B. Chem*. 2012, *173*, 668–675.

[30] Cho, Y.K., Kim, S., Lee, K., Park, C., Lee, J. G., Ko, C., *Electrophoresis* 2009, *30*, 3153–3159.

[31] Green, N. G. and Jones, T. B., *J. Phys. D. Appl. Phys*. 2007, *40*, 78–85.

[32] Gallo-Villanueva, R. C., Sano, M. B., Lapizco-Encinas, B.H., Davalos, R. V., *Electrophoresis* 2013, *35*, 352–361.

[33] Moncada-Hernandez, H., Nagler, E., Minerick, A.R., *Electrophoresis* 2014, *35*, 1803–1813.

[34] Baylon-Cardiel, J.L., Lapizco-Encinas, B.H., Reyes-Betanzo, C., Chávez-Santoscoy, A.V., Martínez-Chapa, S. O., *Lab Chip* 2009, *9*, 2896–2901.

[35] Nili, H. and Green, N.G., *Phys. Rev. E* 2014, *89*, 063302.

[36] Jones, T. and Washizu, M., *J. Electrostat*. 1996, *37*, 121–134.

[37] Wang, X. Wang, X.-B., Gascoyne, P. R., *J. Electrostat*. 1997, *39*, 277–295.

[38] Jackson, J. D, *Klassische Elektrodynamik*, 5th ed. Walter de Gruyter, Berlin, Boston 2013.

[39] Zangwill, A. *Modern Electrodynamics*, 1st ed. Cambridge University Press, Cambridge, New York, Melbourne, Madrid, Cape Town, Singapore, Sao Paulo, Delhi, Mexico City 2013.

[40] Logg, A., Mardal, K.-A., Wells, G., eds., *Automated Solution of Differential Equations by the Finite Element Method*, Lecture Notes in Computational Science and Engineering, Vol. 84, Springer Berlin Heidelberg, Berlin, Heidelberg 2012.

[41] Chen, K. P., Pacheco, J. R., Hayes, M. A., Staton, S. J. R., *Electrophoresis* 2009, *30*, 1441–1448.

[42] Regtmeier, J. Eichhorn, R., Viefhues, M., Bogunovic, L., Anselmetti, D., *Electrophoresis* 2011, *32*, 2253–2273.

[43] Moncada-Hernandez, H., Baylon-Cardiel, J. L., Pérez-González, V. H, Lapizco-Encinas, B. H., *Electrophoresis* 2011, *32*, 2502–2511.

[44] "Please see the supporting documents which are available on the Journal website".